Journal of Materials Chemistry A

ROYAL SOCIETY OF CHEMISTRY

PAPER

View Article Online
View Journal | View Issue

Cite this: J. Mater. Chem. A, 2020, 8, 6740

Electrochemically customized assembly of a hybrid xerogel material *via* combined covalent and non-covalent conjugation chemistry: an approach for boosting the cycling performance of pseudocapacitors†

Taniya Purkait, Dimple, Navpreet Kamboj, Manisha Das, Subhajit Sarkar, Abir De Sarkar and Ramendra Sundar Dey *

Organic quinones conjugated with a conductive support like graphene *via* a covalent and/or non-covalent approach are emerging as low-cost and sustainable alternatives to conventional pseudocapacitive materials because of their fast and reversible redox kinetics. Herein, for the first time, reduced graphene oxide (rGO) networks functionalized with the eco-friendly dopamine (DA) moiety in a combined covalent and non-covalent manner have been explored by a facile hydrothermal synthesis method as high-performance pseudocapacitive materials. Further, a unique *in situ* electrochemical polymerization approach has been undertaken in an attempt to boost the overall storage capacity as well as cycling stability. Electrochemical tuning of the active material can result in an enhancement in the specific capacitance *via* dual improvement in faradaic and capacitive current as compared to the initial xerogel material, highlighting the significance of the *in situ* process. The electrode material shows a highest specific capacitance (C_{SP}) of 348 F g^{-1} at a current density of 0.5 A g^{-1} in 1 M H_2SO_4 while retaining 60% of its initial capacitance even at a very high current density of 200 A g^{-1}. A metal-free all-solid-state symmetric supercapacitor was developed with the *in situ* electropolymerized active material and the as-fabricated device exhibits an excellent C_{SP} of 218 F g^{-1} at 0.325 A g^{-1} in 1 M PVA/H_2SO_4 gel electrolyte with a maximum energy density of 30.3 W h kg^{-1} and power density up to 13 kW kg^{-1}. Most importantly, the material exhibited an extraordinary stability of 53 000 charge–discharge cycles while retaining 94% of its initial capacitance, while the device also shows an excellent capacitance retention of 92% even after 10 000 continuous cycles. Simultaneously, the DFT study was amended to understand the covalent and non-covalent interaction of the redox species, its charge storage mechanism and charge density distribution as well as to calculate the density of states.

Received 3rd March 2020
Accepted 17th March 2020

DOI: 10.1039/d0ta02477e

rsc.li/materials-a

Introduction

Nano-engineered electro-active species are well-known pseudocapacitive materials, but often suffer from poor cycling stability, restricted rate performance and consequently very low power density.[1] Their poor electrical conductivity, and limited resources of expensive inorganic oxides along with complex material engineering of nanostructures hinder these materials from being used for large-scale industrialization.[2,3] Recently, as a new class of electrode materials, organic molecules with electrochemical reversibility[4–8] have emerged as low-cost, renewable and environmentally benign pseudocapacitive species. They are light-weight, easy to synthetically design, and possess large ion-storage capacities beyond those of conventional electroactive metal oxides *via* multi-electron faradaic reactions in a low-molecular-weight charge-storage unit.[9] Among the electroactive organic materials, the quinone species is known to show a fast reversible redox reaction with protons *via* tautomerism in aqueous electrolytes.[10] However, just like other pseudocapacitive materials, poor electroconductivity, slow redox kinetics and poor solubility in common electrolytes also impede the electrochemical performance of these quinone molecules when they are used alone. Therefore, in order to address this problem, organic redox centres have been usually anchored/grafted onto conductive substrates, particularly on carbonaceous materials, *via* a covalent approach[11–15] or non-covalent approach[4,6–9,16] and/or by dissolution in the

Institute of Nano Science and Technology (INST), Mohali-160064, Punjab, India. E-mail: rsdey@inst.ac.in

† Electronic supplementary information (ESI) available: Detailed experimental procedure, formula, SEM, AFM, XPS, Raman, BET, TGA, EDS mapping, computational analysis, Nyquist plot, stability study and other electrochemical data. See DOI: 10.1039/d0ta02477e

experimental electrolyte.[17,18] Unlike transition metal oxides or conducting polymers, these types of hybrid materials often have an interconnected three-dimensional (3D) macroporous xerogel type of structure with stretchability and a low modulus of elasticity. The amount of buffer space available in these highly porous materials can easily alleviate the stress caused by the volume change in redox materials during continuous charge–discharge cycles, leading to an excellent cycling stability.[19,20]

Recently, many researchers have explored non-covalently attaching organic species on a conductive host like graphene as an advanced way to produce electroactive supercapacitors.[4,6–9,16] However, most of the findings have failed to achieve a high cycle lifespan of pseudocapacitors. The non-covalently attached redox species are often loosely bound *via* π–π conjugation, leading to their facile dissolution in the working electrolyte during long service hours and this ultimately results in poor cycling performance.[14] On the other hand, grafting or covalent modification of the conductive substrate may offer enhanced energy storage performance as well as improved stability *via* building well-integrated electronic transport channels, but it evidently decreases the conductivity of the host material. Therefore, to achieve an overall high performance pseudocapacitor with high cycle life, optimization of synthesis engineering is a key step to look into along with the careful selection of electroactive species.

In this work, for the very first time, a combined covalent and non-covalent functionalization approach of reduced graphene oxide (rGO) networks with the eco-friendly dopamine (DA) moiety has been explored *via* a facile hydrothermal synthesis method. The selection of electroactive species here plays a dynamic role in determining whether a covalent or non-covalent functionalization of graphene will take place. The availability of two facile electron donating head and tail groups, *i.e.*, hydroxyl and alkyl amine functionalities at the *para* positions in the DA molecule endorses its easy covalent interaction with the functional groups present on GO at the edge-site during the hydrothermal process, whereas the aromatic π cloud helps in non-covalent interaction with molecular level binding. Covalent functionalization provides electron transport channels with faster charge-transport kinetics, leading to a three-dimensional (3D) interconnected xerogel architecture, while non-covalent functionalization helps in retaining the inherent conductivity of the carbon skeleton. The formation of cross-linkage with interconnected 3D macroporous xerogel architecture has not only been confirmed by various physical characterization experiments, but also supported *via* the first-principles Density Functional Theory (DFT) study. This type of combined interaction helps in retaining the inherent conductivity of the graphene base as the dried dopamine-graphene xerogel (DA-rGO) shows superior electronic conductivity while providing continuous electron transport channels for excellent rate performance. Additionally, DA acts as an efficient spacer element *via* covalent integration, effectively preventing the agglomeration of the rGO sheet, caused by strong π–π interactions.

Furthermore, in this study, we have explored the well-known polymerization tendency of DA to form polydopamine (pDA) at room temperature *via* potential cycling of the xerogel material in the experimental electrolyte and generating the *in situ* electropolymerized pDA-rGO (EpDA-rGO) active material. Potential cycling helps in converting only the non-covalently attached DA moiety into EpDA while the cross-linked DA species remain intact providing channels for electron transport. The *in situ* formation of EpDA-rGO improves the overall active redox sites covering the surface of the carbonaceous base; therefore, proves to be beneficial in terms of achieving enhanced specific capacitance and excellent rate capability, as well as unprecedented cycling stability (53 000 continuous charge–discharge cycles). Additionally, a novel metal-free and self-supported in-plane symmetric solid-state supercapacitor is designed with the EpDA-rGO material, which shows excellent energy density as well as cycling stability (10 000 continuous cycles at a high current density of 10 A g^{-1}) to promote its application in commercialization. The combined output from both the theoretical study and experimental findings helps us to understand that the careful selection of the organic moiety ensures optimum interaction with the conductive substrate which in turn helps in addressing the stability of pseudocapacitors, which is the most critical issue of a commercial supercapacitor.

Experimental

Synthesis of the DA-rGO xerogel

Graphene oxide (GO) was synthesized using a modified Hummers' method, reported elsewhere[21] and described in the ESI (see the Experimental section in the ESI†). Next, the functionalization of the GO and dopamine (DA) moiety was done in a single step *via* an economical hydrothermal method, as presented in Fig. 1a. Briefly, a mixture of as-received DA (Sigma-Aldrich) and GO suspension (1 mg mL^{-1}) was stirred for about 10 minutes to get a homogeneous mixture and then transferred to a Teflon-lined autoclave for 6 hours at 160 °C. The autoclave was cooled to obtain the DA-rGO hydrogel, which was further subjected to lyophilization to get the xerogel architecture. For comparison, gel electrodes composed of polydopamine integrated on rGO sheets (pDA-rGO) were also synthesized using the same experimental conditions. A series of DA-rGO gels were prepared by varying the weight percentages of DA (x) to GO (y) and were labelled according to their initial weight ratios [$x : y = 1 : 1$, $1 : 2$, $1 : 5$, $1 : 10$ and, $1 : 20$]. To understand the role of the DA moiety, only the GO suspension (1 mg mL^{-1}) was subjected to hydrothermal treatment to obtain the rGO hydrogel.

Electrochemical *in situ* conversion of the DA-rGO xerogel to EpDA-rGO

The as-synthesized DA-rGO sample was used as a conductive ink to be drop-cast on a glassy carbon (GC) electrode to test its electrochemical performance as a storage material. In order to obtain the optimized electro-active material, however,

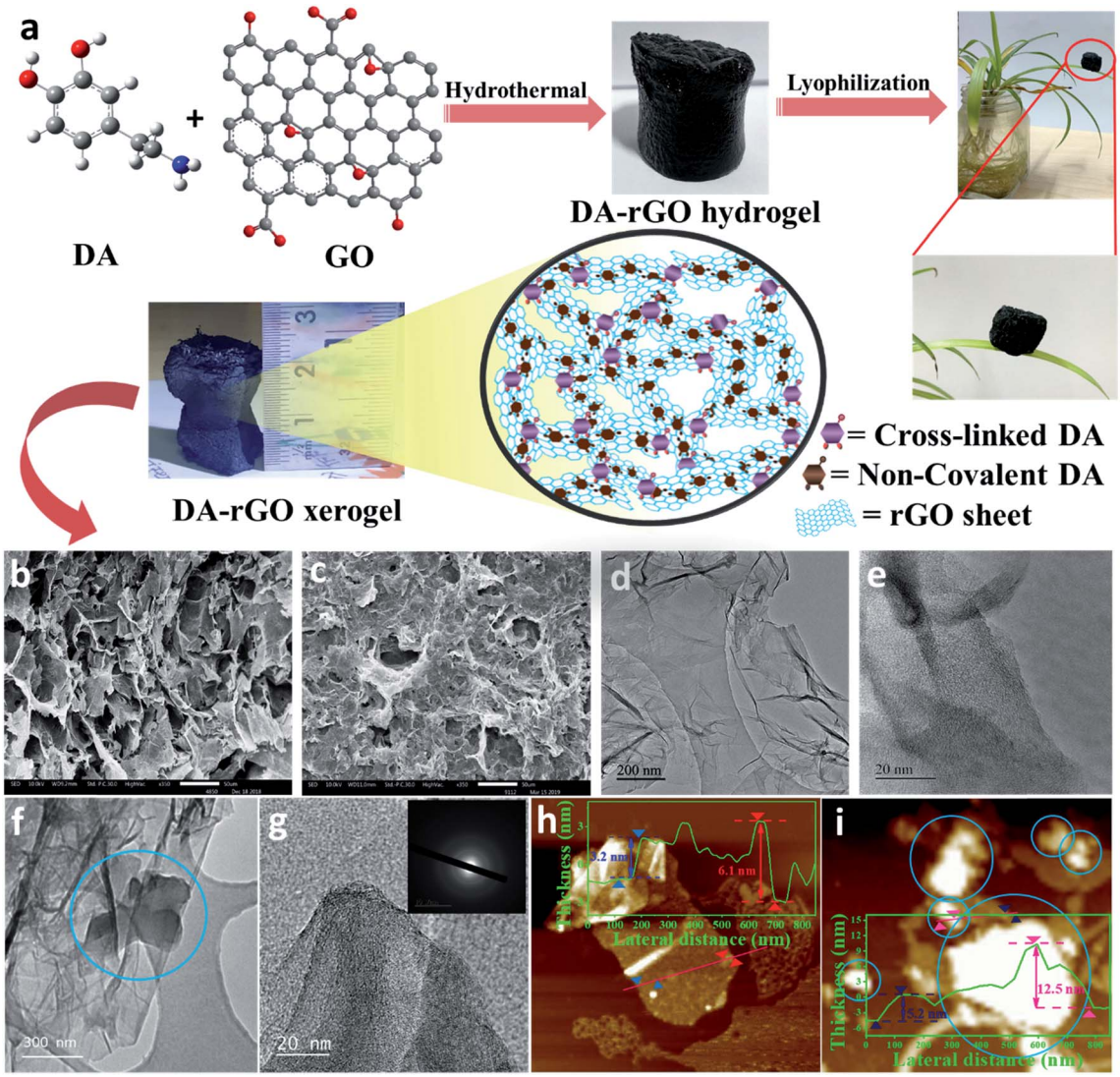

Fig. 1 (a) Schematic representation of the hydrothermal synthesis of the dopamine (DA) based reduced graphene oxide (rGO) xerogel (DA-rGO). Surface analysis of the optimized xerogel material, DA-rGO$_{1-2}$ as well as the *in situ* electropolymerized active material, EpDA-rGO by various microscopic techniques; (b) SEM image of DA-rGO showing the interconnected 3D porous architecture. (c) SEM micrographs after electropolymerization revealing increased surface coverage *via* $\pi-\pi$ interactions. (d) and (e) TEM and corresponding HRTEM images of the xerogel, DA-rGO. (f) TEM analysis of EpDA-rGO clearly showing large chunks of dark patches (marked by blue circles) revealing the presence of the polymer on the rGO matrix. (g) Related HRTEM image, the inset showing the SAED pattern. (h) AFM study at different positions of a single DA-rGO xerogel flake, the inset showing how the thickness profile varies with the presence of DA (bright spots) on the rGO sheet. (i) AFM analysis confirming the surface coverage of rGO by EpDA with increased bright spots and the inset shows an enhanced thickness of the sheets.

potential cycling was performed at a scan rate of 100 mV s^{-1} for 100 cycles in the working electrolyte of 1 M H_2SO_4. The *in situ* conversion of non-covalently attached DA species to pDA *via* electrochemical oxidation and rearrangement was observed and the final active material, EpDA-rGO, was further tested for its electrochemical behaviour. On the other hand, another control sample was prepared by taking the aforementioned hydrothermally reduced GO (rGO) and DA in solution (in a similar weight percentage of the hydrothermally optimized xerogel) and drop-casting it on a glassy-carbon electrode in an attempt to electrochemically cross-link the DA moiety with the rGO skeleton. The sample was denoted as rGO/DA.

Results and discussion

Physical characterization

DA-rGO was prepared by the functionalization of graphene oxide (GO) *via* the dopamine (DA) moiety, in a single step *via* an economical hydrothermal method, as presented in Fig. 1a (for details, please see the Experimental section). Simultaneously, in this work, we introduced a unique *in situ* electropolymerization technique to obtain the optimized electro-active material. The as-synthesized DA-rGO sample was subjected to potential cycling at a scan rate of 100 mV s^{-1} for 100 cycles in the working electrolyte of 1 M H_2SO_4 to obtain the final active material, EpDA-rGO (Experimental section).

Surface morphological characterization of the obtained DA-rGO xerogels was performed using a scanning electron microscope (SEM) (Fig. 1b and S1a–h, ESI†). As shown in Fig. 1b, the freeze-dried DA-rGO$_{1-2}$ has an interconnected 3D macroporous hierarchical framework with pore sizes ranging from submicrometers to several micrometers. The SEM images of the other synthesized xerogels are also presented in Fig. S1a–h, ESI,† which also support the 3D porous interconnected morphology of the xerogel. The surface morphological inspections were further extended to study the effect of *in situ* electropolymerization in the experimental electrolyte on the optimized xerogel structure. Fig. 1c exhibits the SEM micrographs of the EpDA-rGO surface, which shows a similar interconnected architecture to that of DA-rGO, but with more surface coverage. The intensity of the non-covalent π–π interaction may have increased several fold after electropolymerization as compared to only the xerogel material, resulting in more surface coverage of the rGO matrix by EpDA. Transmission electron microscopy (TEM) was adopted to further study the surface interaction of the DA molecule with the overlapping graphene sheets. Interconnected graphene sheets (Fig. 1d) with wrinkles outlining the sheets by DA are clearly visible in the high-resolution TEM (HRTEM) images, as exhibited in Fig. 1e. This kind of open-structured hybrid network provides easy accessibility to the electrolyte ions from both sides of the sheets for rapid charge transport through the electronic channels provided by the amide cross-linkage of DA molecules. Interestingly, in the TEM analysis (Fig. 1f and g) of the EpDA-rGO material, intense dark patches are observed, which are highlighted by blue circles, confirming the increased non-covalent π–π interaction between the polymer and the rGO matrix. The selected area electron diffraction (SAED) analysis (Fig. 1g, inset) in TEM measurements reveals the absence of any characteristic lattice points corresponding to the hexagonal lattice of crystalline graphene, indicating that crystallinity is substantially decreased after inclusion of the DA moiety in the rGO matrix. After *in situ* polymerization, which substantially improves the coverage of the rGO surface, the crystallinity of the rGO matrix is further reduced. Surface topographic analysis by atomic force microscopy (AFM) further confirms the formation of the cross-linked xerogel structure. As displayed in Fig. 1h, a single DA-rGO flake with DA at the edge as well as on the rGO backbone can be seen. The height profile reveals the sheets with an average height of 3–6 nm (inset of Fig. 1h), which is much higher as compared to that of a single GO sheet (0.9 nm), as exhibited in Fig. S2a and b, ESI.† Detailed surface topological characterization of the EpDA-rGO material by AFM (Fig. 1i) also ensures *in situ* polymerization with an enhanced presence of bright spots (EpDA) almost covering the rGO sheets beneath. The AFM height profile at various positions on the EpDA-rGO surface, displayed in the inset of Fig. 1i, reveals that the average sheet height increased to around 5–12 nm, as compared to only DA-rGO (Fig. 1h, inset); confirming the *in situ* electropolymerization.

To investigate the successful reduction of the precursor (GO) in the xerogel material (DA-rGO), X-ray diffraction (XRD) analysis was employed and the results were compared to those of pristine hydrothermally reduced GO (rGO) without incorporating DA. Further inspection of the xerogel structure after its *in situ* electropolymerization was also performed to follow any change in its graphitic domain. As can be seen in Fig. 2a, the diffraction peak at $2\theta = 11.96^\circ$ corresponding to the (100) graphitic plane of GO completely disappears in the XRD spectra of rGO and DA-rGO as well as EpDA-rGO materials, suggesting that GO is completely reduced in the xerogel material during hydrothermal treatment and the structure is retained even after *in situ* electropolymerization in the experimental electrolyte. The presence of characteristic diffraction peaks at $2\theta = 30.2^\circ$, corresponding to the (002) graphitic plane and $2\theta = 43^\circ$, corresponding to the (110) graphitic plane ensures the removal of most of the oxygen functionalities present in GO in rGO, DA-rGO and EpDA-rGO, respectively.

Fourier transform-infrared (FT-IR) spectroscopic analysis was carried out *via* the attenuated total reflection (ATR) technique to confirm the grafting of DA on the rGO sheet *via* covalent functionalization. All the FTIR-ATR peaks of DA, rGO and, DA-rGO are identified and assigned to the corresponding characteristic bands, as summarized in Table S1.† As displayed in Fig. 2b, the characteristic bands of the quinonic backbone (1252 and 863 cm^{-1}) is clearly visible in the xerogel structure.[22] A broad peak at 3460 cm^{-1} appears due to the O–H vibration.[23] Additionally, the appearance of a peak at 1727 cm^{-1} corresponding to the stretching frequency of the carbonyl functional group along with shifting in the N–H bending vibration (from 1612 cm^{-1} to 1652 cm^{-1}) from the pure DA moiety[24] ensures the formation of an amide linkage in DA-rGO. The additional C–H stretching vibration, assigned to the peaks obtained at 2930 cm^{-1} and 2854 cm^{-1} corresponds to the aromatic and alkane C–H stretching frequency of the linkage group as well as the conjugated rGO architecture at the base of the xerogel.[25]

To obtain a more clear understanding about the nature of chemical bonding between DA and rGO and the subsequent changes occurred to the xerogel structure after *in situ* polymerization, X-ray photoelectron spectroscopic (XPS) analysis was adopted. The overall spectra of DA-rGO in Fig. 2c ensure the presence of the requisite elements, C, N and O with an atomic percentage of 83%, 4% and 13% respectively in the DA-rGO xerogel material, while the elemental N percentage dramatically improves to 8.4% in the EpDA-rGO structure. Compared to the precursor material, GO, the atomic percentage ratio of carbon to oxygen increases in DA-rGO, confirming the reduction of GO to rGO, as revealed in Fig. 2c. However, EpDA-rGO exhibits a slightly higher O content as compared to DA-rGO and an additional peak for S, which may arise due to the continuous CV cycling in the experimental electrolyte of 1 M H_2SO_4. The high-resolution deconvoluted C1s spectra of the DA-rGO xerogel material, shown in Fig. S3a,† disclose three characteristic peaks at 284.5 eV, 286.2 eV and 288.9 eV corresponding to the C–C, C–N and C=O bonds, respectively.[26] Similarly, as expected, the deconvoluted C1s spectra of EpDA-rGO, displayed in Fig. S3b,† reveal three different binding energies, peaking at 284.6 eV, 286.2 eV and 288.1 eV, with only a slight shift in the peak positions, corresponding to the C–C, C–N and O–C=O bonds, respectively.[26] The deconvoluted N1s

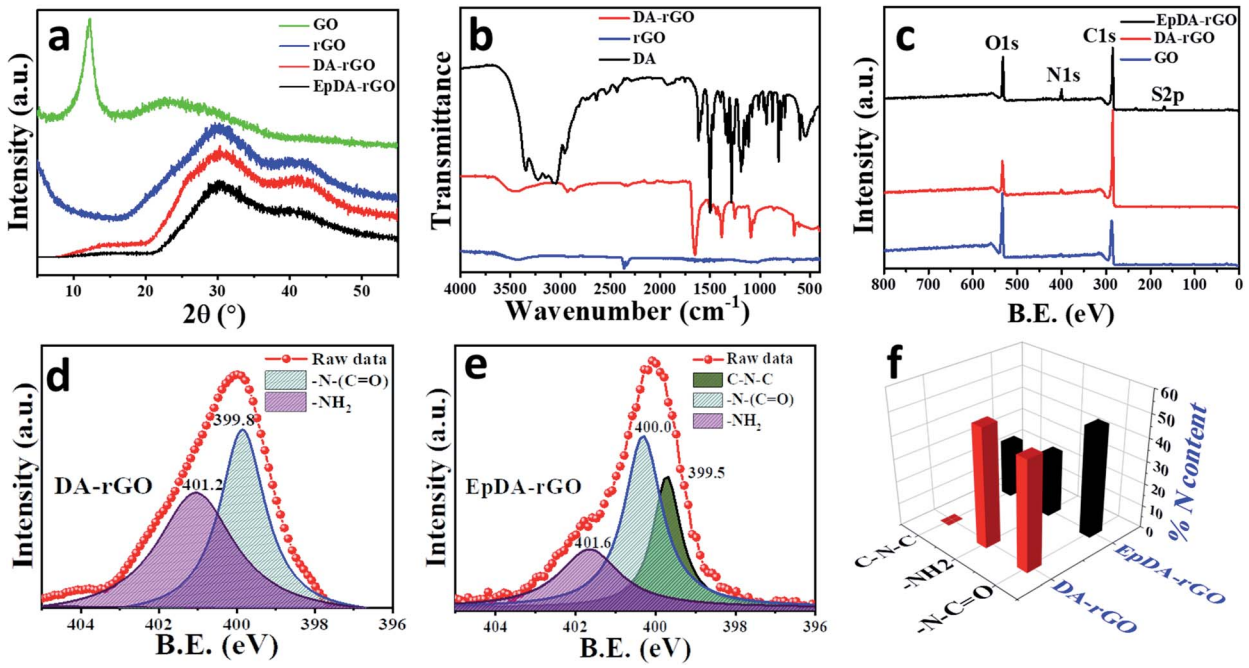

Fig. 2 (a) XRD patterns of the xerogel before and after its *in situ* electropolymerization as compared to GO and rGO. (b) Comparative FTIR analysis of the optimized xerogel with respect to DA and rGO, showing successful incorporation of the DA moiety into the rGO matrix. (c) Relative XPS analysis of EpDA-rGO and DA-rGO as compared to GO. Deconvoluted N1s spectra obtained from high-resolution XPS analysis of (d) DA-rGO and (e) EpDA-rGO. (f) Different types of nitrogen environments in the DA-rGO and EpDA-rGO samples and their relative percentage highlighting the *in situ* electropolymerization process.

spectra (Fig. S3b† and 2e) were instrumental in determining the binding preference in the hydrothermally obtained xerogel structure and the *in situ* electropolymerized active material, respectively. The spectra corresponding to DA-rGO (Fig. S3b†) were fitted to two peaks at 399.9 eV and 401.2 eV, respectively. The peak at 399.9 eV was assigned to the amide groups (–N–C=O) which confirms the occurrence of covalent cross-linking in the hybrid structure,[27] while the peak assigned to 401.2 eV indicates the presence of primary amine (R-NH_2), which ensures the presence of non-covalently attached DA species.[28] On the other hand, N1s spectra (Fig. 2e) of EpDA-rGO were fitted to three distinct characteristic peaks at 399.5, 400.0 and 401.2 eV corresponding to substituted amines (C–N–C), amide groups (–N–C=O), and free –NH_2 groups.[25] As expected, the peaks corresponding to –N–C=O and R–NH_2 groups in DA-rGO were slightly shifted or remained constant after electropolymerization. However, a significant change is observed in the N 1s core level spectrum *via* the appearance of C–N–C binding energy at 399.5 eV due to the rearrangement of the non-covalently attached free amine groups into a 5-membered heterocyclic ring (leucodopaminechrome or dopaminechrome species) during the electropolymerization process.[25,29] To quantify the relative percentage of the (i) covalent and non-covalent attachment of dopamine to the hybrid material and (ii) amount of DA which has been transformed to EpDA during the polymerization process, we have extracted the %N content from the deconvoluted N1s spectra and presented in Fig. 2f. The %N content from the covalently attached (–N–C=O) amide linkage remains almost similar before (~48% for DA-rGO) and after (~47.7% for EpDA-rGO) the polymerization process. However, the %N content in non-covalently attached free –NH_2 groups present in DA-rGO (~52%) gets split into C–N–C (~24.5%) and –NH_2 (~27.8%) binding energies in EpDA-rGO. This confirms the *in situ* electropolymerization process as well as quantifies the percentage of DA-rGO still present and EpDA-rGO formed after the electropolymerization process.

Raman spectral analysis was conducted to investigate the structural transformation during hydrothermal treatment as well as after electropolymerization. Fig. S4† displays the characteristic D and G bands of graphitic carbon, which appears at ~1348 and ~1589 cm^{-1}, respectively for GO, rGO, DA-rGO and EpDA-rGO structures. As expected, the intensity ratio of I_D/I_G decreases from GO (1.21) to rGO (1.1) because of the restoration of the graphitic domain. However, in the xerogel structure, the intensity ratio once again increases to 1.25, indicating expansion of the conjugated backbone *via* covalent functionalization with DA.[14] The I_D/I_G ratio remains almost intact at 1.26 in the EpDA-rGO xerogel material, indicating retention of the graphitic structure even after polymerization.

The N_2 adsorption/desorption analysis (Fig. S5†) was carried out to study the specific surface area (SSA), and pore size distribution as well as pore volume. The sorption isotherm displays typical type-IV behaviour with a specific surface area of 105 $m^2\ g^{-1}$. The obvious hysteresis loop in the range of P/P_0 = 0.4–0.9 and the sharp increase of the adsorption amount at P/P_0 > 0.9 indicate the existence of a large number of mesopores in DA-rGO. As expected, an abundance of micropores (~2 nm) along with mesopores (6–12 nm) can be observed in the inset of

Fig. S5,† as calculated by the Barrett–Joyner–Halenda (BJH) pore size distribution method. The total pore volume of 1.28 $cm^3 g^{-1}$ clearly demonstrates the high mass loading of DA on the rGO sheets, a prerequisite for obtaining a high gravimetric capacitance of pseudocapacitive electrodes.

To determine the extent of DA distribution in the DA-rGO xerogel and the distribution of EpDA in the sample after polymerization, EpDA-rGO on the porous rGO network, elemental mapping was carried out *via* energy dispersive X-ray spectroscopy (EDS). Uniform distribution of all the elements, *i.e.*, carbon, oxygen and, nitrogen, can be clearly observed in Fig. S6a† as well as in Fig. S6b.† Individual elemental contributions are exhibited in Fig. S6c–h.† A close look at Fig. S5a† indicates the abundance of elemental nitrogen on the periphery of the interconnected pores, which highly supports our finding that DA acts as a cross-linker here. The elemental distribution once again substantiates the adequate incorporation of the DA moiety into the DA-rGO structure. On the other hand, the increased percentage of elemental N can be clearly observed because of the enhanced non-covalent interaction with the polymer (Fig. S6b†), which is in close accordance with our XPS results.

Thermogravimetric analysis (TGA) was carried out (Fig. S7†) to compare the thermal stability of different electrode materials in an air atmosphere at a heating rate of 10 °C min^{-1}. GO is thermally unstable and rapid mass loss occurs in two steps. The 15% mass loss observed for GO at ~100 °C is ascribed to the loss of adsorbed water molecules or sublimation whereas the 40% mass loss at ~200 °C can be due to the loss of labile oxygen-containing functional groups.[30] In contrast, rGO withstands much higher temperature because of the removal of the most of the functional groups. It shows a very gradual decrease in the weight loss at varying temperatures, consistent with previous reports.[30] Comparatively, DA-rGO and EpDA-rGO show much better thermal stability than rGO and GO in the temperature range of 40–550 °C. As can be seen in the inset of Fig. S7,† EpDA-rGO and DA-rGO show almost 96% and 92% mass retention, while GO and rGO can retain only about 36% and 84% of the initial sample mass at 400 °C. DA is a synthetic mimic of a mussel adhesive protein and it shows almost no decomposition up to ~230 °C; then starts to degrade a little up to 300 °C due to the loss of the catechol moiety. The second thermal decomposition occurs in the range of 300–500 °C, most likely due to the decomposition of the alkyl spacer and the amide group.[31] This indicates that DA contains necessary thermal stability for incorporation into the composite xerogel material, DA-rGO. It was observed that the composite material, DA-rGO follows a similar decomposition path as well but with higher decomposition temperature. This once again may be attributed to the synergistic thermal stability of both rGO and DA in the composite xerogel material due to the stronger π–π interaction. The first decomposition occurs in the range of 350–550 °C while the 2nd thermal degradation occurs in the range of 550–680 °C. After *in situ* polymerization, the EpDA-rGO expectedly follows a similar thermal decomposition pathway, however the % mass retention significantly improves to 41% from 16% in DA-rGO after complete decomposition of the functional moieties takes place at ~680 °C. This once again indicates that the *in situ* polymerization of the xerogel moiety in the experimental electrolyte greatly improves the thermal stability of the electrode material.

Furthermore, in order to promote the xerogel material as a potential option to be employed for energy storage, the electrical conductivity of all the active electrode materials was determined with a source meter *via* a two-probe method, while GO shows a very small conductivity of 0.77 mS cm^{-1}; after removal of functional groups, the conductivity in hydrothermally derived rGO improves to 5.35 S cm^{-1}. Interestingly, after the xerogel formation, DA-rGO exhibits an excellent electrical conductivity of around 81 S cm^{-1}, which was slightly improved in EpDA-rGO (82.6 S cm^{-1}) after *in situ* polymerization.

Computational methodology and studies

In order to shed light on the preferred orientation of the redox moiety, DA and its conjugation chemistry with the graphene sheet, DFT calculations have also been performed. The charge density distribution in the preferred orientations as well as the role of density of states (DOS) in the charge storage mechanism was investigated in detail for an atomic-scale insight. Therefore, to unveil the mechanism underlying the conjugation, binding energy has been calculated, at first, for different possible conformations or orientations of the redox moiety at different adsorption sites of DA, including non-covalent binding to the graphene sheet (both in vertical and parallel conformations). The possibility for adsorption in a cross-linking conformation (*i.e.*, covalent interaction during charge-storage) has also been explored. The structure of the DA molecule was optimized first and then it was adsorbed on rGO in various conformations for further structural optimizations of the combined system, DA-rGO. The total energy calculations for the DA molecule were performed with DFT as implemented in the Gaussian16 package.[32,33] Fig. S8† shows the relaxed structure of the DA molecule, which is in good agreement with the earlier reports.[34]

In the next step, the binding energies of the DA molecule to the rGO sheet were calculated at different possible sites (shown in Fig. S8†). The calculated binding energy (E_b) is defined as follows:

$$E_b = E_{(rGO+DA)} - (E_{rGO} + E_{DA})$$

Here, $E_{(rGO+DA)}$ is the total energy of reduced graphene oxide with an adsorbed DA molecule, E_{rGO} is the total energy of reduced graphene oxide and E_{DA} is the total energy of the DA molecule. Fig. S9† exhibits different optimized geometries of the DA molecule, which is oriented parallel (P_1 and P_2) and vertical (V_1, V_2 and, V_3) to the rGO sheet. Based on binding energies calculated for various orientations (Table 1) in non-covalent interactions, the most stable adsorption conformation is found to be the one of its horizontal orientation relative to the rGO sheet, as confirmed by the highest binding energy, thereby suggesting the highest likelihood of charge transfer in this parallel orientation.

However, interestingly, when DA was chosen as a cross-linker in binding adjacent rGO sheets, the binding energy of

Table 1 Binding energies of DA at various alignments on the rGO sheet

	Cross-linking	P_1	P_2	V_1	V_2	V_3
B.E. of DA onto rGO (eV)	3.39	0.3519	0.3166	0.2058	0.2256	0.34

the covalently linked structure was found to be even higher (Table 1). Fig. 3a and b show the top and side view of the assembly of rGO sheets *via* the amide linkage with the DA molecule. Here, the dopamine (DA) molecule acts as a linker with a high binding energy of −3.39 eV and plays an important role in assembling the rGO sheets. One end of DA forms the amide (–CO–NH–) linkage with the –COOH of the rGO whereas its other end connects *via* O-atoms (by eliminating the $2H_2O$/DA molecule) to the C-atom of rGO. This further substantiates our proposed mechanism of DA serving as a cross-linker in forming the 3D interconnected macroporous structure.

Furthermore, we attempted to ascertain the origin of the larger strength of interaction for DA molecules on the graphene surface in the parallel conformation, when both the moieties are super-imposed on each other (P_1) (Fig. 3c and d). A larger charge re-distribution on rGO is caused by DA in the P_1 position on account of the perfect alignment of the π-cloud of rGO on DA due to the availability of oxygen atoms in rGO with the primary amine group of DA as shown in Fig. 3c and d, leading to larger charge distribution.

In addition, the total DOS for pristine rGO and DA-rGO in both parallel and vertical orientations has been calculated (Fig. 3e). The DOS profile shows a large increase in the density of states in DA-rGO with respect to rGO around the Fermi level. These electronic states will take part in current conduction upon the application of bias voltage and thereby contribute to an enhanced conductivity relative to rGO. Compared to previously reported redox-based graphene systems,[6] the peaks observed in the present case lie much higher than the Fermi level. These empty bands help in providing more capacitance to store charges. This clearly implies that the pseudocapacitance mainly originates from the carbonyl groups of the hybrid structure, which is consistent with the proposed mechanism.

Electrochemical characterization

Electrochemical conversion of DA-rGO to EpDA-rGO. The DA moiety is known for its ease of polymerization under ambient conditions and leads to the formation of the pDA layer *via* 5,6-dihydroxyindole formation after molecular rearrangement (Fig. 4).[35] The pDA having a much enlarged π charge cloud as

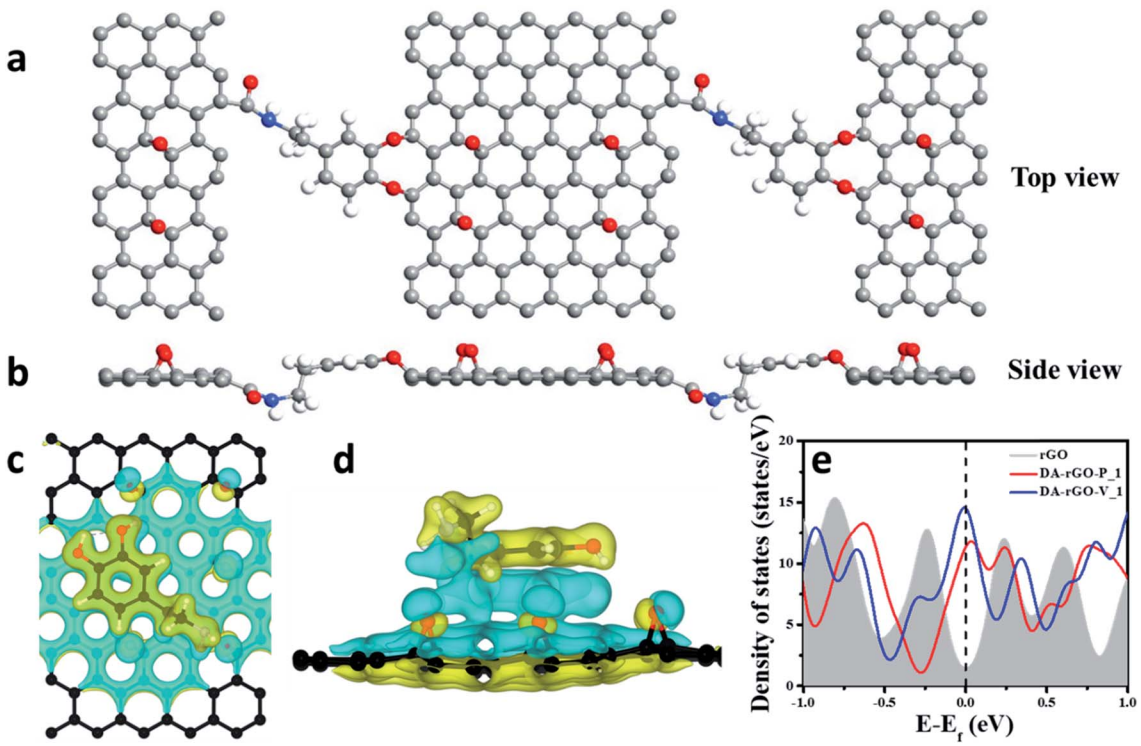

Fig. 3 (a) Top and (b) side view of the assembly of rGO sheets *via* the amide cross-linkage with DA molecules calculated by DFT calculations. (c) Top and (d) side view of the charge density difference plot of the DA molecule over the rGO sheet (at the highest binding-energy site assigned as P_2). Charge accumulation and depletion are represented by the yellow and cyan regions, respectively. The iso-surface level is ±0.07 e $Bohr^{-3}$. (e) Total density of states (DOS) for pristine rGO and DA-rGO in the parallel as well as vertical stacked position.

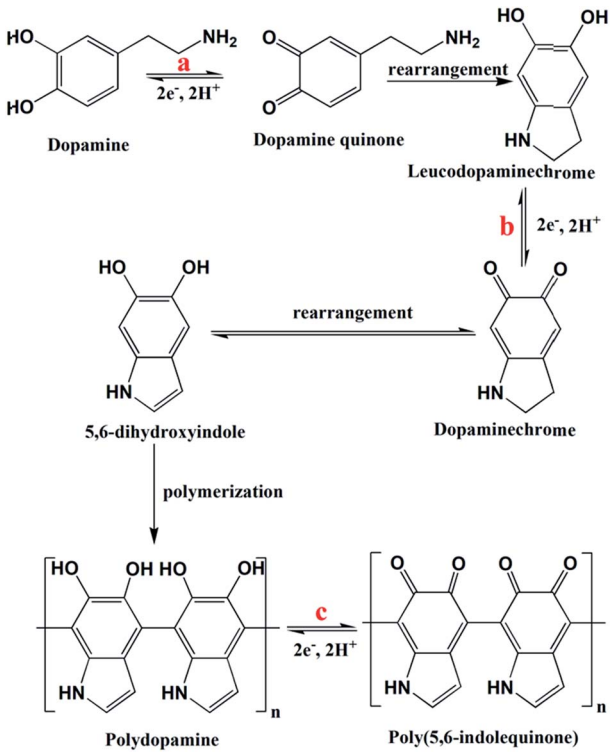

Fig. 4 Proposed reaction mechanism of DA-rGO to *in situ* EpDA-rGO during potential cycling.

compared to only DA can participate in the non-covalent π–π conjugation in a more efficient way and consequently lead to more surface coverage of the conductive rGO structure or more mass-loading. We took advantage of this simple conjugation chemistry by potential cycling of the DA-rGO electrode material in the experimental electrolyte at a scan-rate of 100 mV s^{-1} leading to the formation of the *in situ* EpDA-rGO structure on the electrode surface. Fig. S10† displays continuous 100 cyclic voltammetric (CV) cycles showing a gradual shift in the characteristic redox (oxidation) peaks from DA (0.75 V and 0.6 V) to EpDA (0.6 V and 0.42 V), while the increase in the capacitive response was also observed. The proposed reaction process of EpDA formation from DA is outlined mechanistically in Fig. 4 and schematically in Fig. 5a. The oxidative redox peaks (0.6 V and 0.75 V) corresponding to the two $2e^-$ transfer processes before the potential cycling can be ascribed to (i) dopamine to dopaminequinone formation ('a' in Fig. 4) and, (ii) leucodopaminechrome to dopaminechrome formation ('b' in Fig. 4), respectively,[35,36] while, after the potential cycling, the two distinct redox peaks (0.6 V and 0.42 V) correspond to the $2e^-$ transfer processes, namely – (i) dopamine to dopaminequinone formation ('a' in Fig. 4) and, (ii) polydopamine to poly(5,6-indolequinone) formation ('c' in Fig. 4), respectively.[35] As illustrated in Fig. 5a, the molecular structures of the electrode surface, before and after potential cycling, clearly show that the non-covalently (π–π interaction) attached DA moiety (brown coloured) gets converted to pDA molecules (orange coloured) anchored on the rGO sheet, while the covalently (*via* amide linkage) linked DA moieties (purple coloured) remain intact; in accordance with our XPS quantification (Fig. 2e). Cyclic voltammograms of the electrode material before and after potential cycling, at a scan rate of 1 mV s^{-1}, are exhibited in Fig. 5b in order to showcase the role of electrochemical polymerization in the overall capacitance enhancement of the pseudocapacitor electrode. A characteristic cathodic peak (at 0 V) corresponding to the dopaminechrome to leucodopaminechrome reduction,[35] which appears in DA-rGO, but subsequently disappears or gets potential shifted during continuous cycling in EpDA-rGO (Fig. 5b) also supports the *in situ* electropolymerization process. In order to optimize the active material mass-loading, a number of mass-loading experiments were carried out *via* CV at various scan rates. The effect of mass loading on the gravimetric (Fig. S11a†) as well as areal (Fig. S11b†) capacitance of the electrode at various sweep rates was investigated and depending on the rate retention capability, the optimized mass-loading was found to be 1 mg cm^{-2}. Since, a highest rate capability of ~75% is attained with a mass-loading of 1 mg cm^{-2} as compared to other active mass-loadings (0.5, 1.2, 2, 4 mg cm^{-2}); this particular mass-loading was maintained throughout the electrochemical testing of the electrode material.

Determination of capacitive contribution in DA-rGO and EpDA-rGO electrodes. In order to quantitatively measure the enhancement in overall capacitance after the *in-operando* electropolymerization process, we conducted detailed deconvolution of the cyclic voltammograms of both DA-rGO and EpDA-rGO electrodes. CVs were recorded at various scan rates for both the electrodes in order to determine the dominant charge-storage phenomenon, *i.e.*, whether it is a diffusion-controlled or surface-confined redox process.[37,38] By following equations described in the ESI† (eqn (5) and (6)), it was observed that the surface-confined process strictly controls the charge-transport kinetics in both the electrodes. As observed in Fig. 5c, cyclic voltammograms of the EpDA-rGO electrode exhibit a pseudocapacitive nature with reversible redox peaks at a sweep rate of 10–200 mV s^{-1}. The flat ends of the CV curves (−0.1 V to 0.9 V) can be attributed to the non-faradaic contribution from the rGO skeleton. Retention of the CV shape even at higher scan rates only indicates the excellent mechanical stability of the electro active xerogel architecture. At lower sweep rates, the redox peaks are much more prominent, however, with increasing scan rate, the contribution from the faradaic process decreases, leading to smaller redox humps, consistent with other reported pseudocapacitive electrodes.[6] The inset of Fig. 5c demonstrates that the arbitrary function, 'b' (in eqn (5) in ESI†) for both DA-rGO (0.92) and EpDA-rGO (0.95) approximates to 1, clearly indicating that the stored charge changes linearly with the sweep rate, meaning a surface confined process.[39,40] To determine the impact of *in situ* polymerization on the capacitive properties, the change in mass transport was additionally measured for these surface-confined redox processes. The surface coverage of the rGO skeleton *via* both DA and EpDA was calculated (following eqn (11) in the ESI†) to be 0.48×10^{-9} mol cm^{-2} and 1.15×10^{-9} mol cm^{-2}, respectively. This clearly indicates that after electropolymerization, the surface coverage of the rGO with the

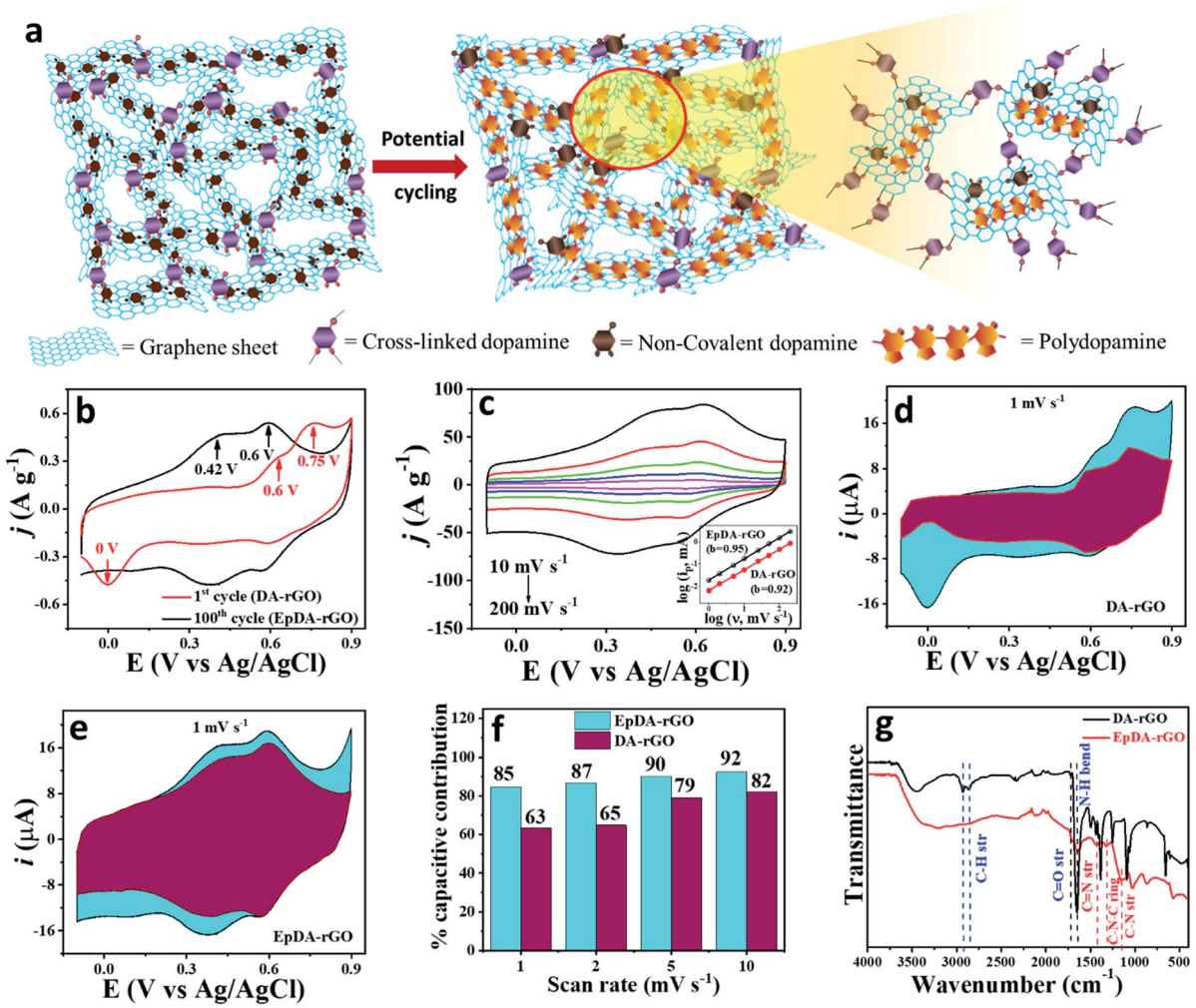

Fig. 5 (a) Schematic demonstration of the 3D DA-rGO cross-linked xerogel and its subsequent polymerization to EpDA-rGO after potential cycling; magnified image showing the *in situ* EpDA-rGO sheets through both covalent and non-covalent linkage. (b) CV at a scan rate of 1 mV s^{-1} of DA-rGO showing contribution to faradaic capacitance (red curve) caused by loading of DA, and improvement in overall capacitance (black curve) caused by a simple *in situ* electrochemical conversion to EpDA. (c) Highly reversible cyclic voltammograms of EpDA-rGO at various scan rates; the inset showing the log *i vs.* log *ν* plot of the anodic peak currents at 0.6 V for both DA-rGO and EpDA-rGO. (d)–(f) Quantitative capacitive analysis of the charge storage process of both DA-rGO and EpDA-rGO electrodes and their comparative study; the capacitive (purple) and faradaic (bright cyan) contribution of (d) DA-rGO and (e) EpDA-rGO at a sweep rate of 1 mV s^{-1}. (f) The ratio of capacitive contribution to the overall capacitance at various scan rates. (g) FTIR-ATR spectra showing generation of characteristic peaks of EpDA after electrochemical cycling.

redox species increases because of a certain increase in the active redox sites. Additionally, in Fig. 5d and e, the voltammetric response for the capacitive current (purple shaded region) is compared with the total measured current (bright cyan shaded region) at a very low scan rate of 1 mV s^{-1}, for both DA-rGO and EpDA-rGO, respectively (following eqn (7) and (8) in ESI†). Slow sweep rates are preferred in order to provide the conditions in which the contribution from faradaic non-capacitive processes is at maximum.[8] As can be observed in Fig. 5d, the ratio of the capacitive charge storage to the total charge storage is 63% only for the DA-rGO electrode, while the capacitive contribution of EpDA-rGO to the overall current greatly improves to 85% which is extremely high, and demonstrates the high rate capability of the system (Fig. 5e). The rate of improvement in capacitive contribution with increasing scan-rate is summarized in Fig. 5f in the form of a bar diagram for both DA-rGO and EpDA-rGO electrodes, which reveals the superior performance of the electrode after polymerization in terms of both enhanced specific capacitance as well as improved rate capability. This enhancement in capacitive contribution very clearly demonstrates the significance of our unique *in situ* polymerization process. The unprecedented improvement in the overall charge storage after electropolymerization may be ascribed to the following factors: (i) the obvious increase in the π–π interaction of EpDA to rGO after polymerization is helping in the increment of the non-faradaic capacitive current, while (ii) some free DA species which did not take part in the polymerization process will still participate in the $2e^{-}$–$2H^{+}$ coupled redox processes along with EpDA, as evidenced by the clear presence of the redox peak at 0.6 V, ascribed

to the dopamine quinone formation from dopamine ('a' in Fig. 4). The combined input from both these redox species (DA and EpDA) contributing to the enhancement of the faradaic contribution along with the increment in the capacitive current due to the improved surface coverage of rGO by EpDA is solely responsible for the dramatic improvement in electrochemical performance.

The change in the electrode active material structure was also confirmed by the FTIR-ATR analysis (Fig. 5g). The disappearance of the alkane C–H stretching frequency (2860 cm^{-1})[23,25] of DA-rGO in the EpDA-rGO structure clearly indicates the formation of the 5-membered ring in 5,6-dihydroxyindole *via* rearrangement, as described in Fig. 4. An intense peak corresponding to the N–H bending[39] frequency of the π-conjugated free DA species on the rGO sheet in DA-rGO almost vanished in the EpDA-rGO structure, confirming the polymerization process. On the other hand, several important characteristic stretching frequencies appear in the FTIR-ATR analysis of the EpDA structure, for example –C═N stretching (1427 cm^{-1}),[41,42] C–N stretching in secondary amine (1152 cm^{-1}),[41,43] C–N–C ring vibration (1368 cm^{-1}),[25] *etc.* which confirms the formation of *in situ* EpDA during potential cycling. The *in situ* polymerization not only helps in better π–π conjugation and contributes to higher overall capacitance as compared to only the DA-rGO xerogel material, but is also responsible for improved cycling stability by preventing the loss of loosely bound DA species from the hybrid structure. In order to get the composition-dependent charge-storage capacity, the cyclic voltammogram of the EpDA-rGO electrode was compared with those of pristine GO and rGO modified electrodes at a scan rate of 100 mV s^{-1}, as shown in Fig. S12a.† EpDA-rGO electrodes show much-expanded CVs (150 times higher C_{SP} than GO and 10 times higher C_{SP} than rGO, respectively) with pronounced redox peaks due to the *in situ* electrochemical conversion after potential cycling. To understand the shift in the characteristic redox peaks in EpDA-rGO as compared to DA-rGO, chemically synthesized (similar hydrothermal treatment) pDA anchored on the rGO sheet (denoted as pDA-rGO) was also studied for its capacitive behaviour. Although similar oxidation peaks (centered at 0.42 V and 0.6 V) are observed in the pDA-rGO electrode, the decreased area under the CV curve (1.5 times lesser C_{SP}) clearly demonstrates the advantage of the *in situ* electrochemical conversion process. Another electrode was also modified with rGO and DA aqueous solution (denoted as rGO/DA) to see whether the DA-rGO hybrid can be achieved electrochemically. But as exhibited in Fig. S12a,† there is an insubstantial current response in the rGO/DA electrode, which may be due to the presence of the loosely absorbed DA moiety only at the rGO surface and clearly an absence of any potential interaction between DA and rGO. This observation promotes the advantage of the economical hydrothermal method followed by potential cycling. In order to further establish the advantage of our facile hydrothermal synthesis method followed by novel *in situ* electropolymerization, another pure EpDA-rGO electrode was fabricated, following methods reported in the literature. Typically, the hydrothermally derived rGO material was subjected to potential CV cycling in the experimental electrolyte containing 1 mg mL^{-1} DA for obtaining the pure EpDA-rGO electrode. As can be seen in Fig. S12b† (magnified version of Fig. S12a†), the as-obtained pure EpDA-rGO electrode material exhibits specific capacitance (C_{SP} = 33 F g^{-1}) in the range of that of the hydrothermally obtained rGO electrode (C_{SP} = 27 F g^{-1}); whereas our optimized EpDA-rGO electrode (C_{SP} = 263 F g^{-1}) shows much higher specific capacitance. This once again substantiates the importance of the facile hydrothermal synthesis method that helps in covalently linking the DA species onto the rGO skeleton and helps in improving the overall capacitance of the composite material drastically.

To demonstrate the effect of DA loading on the capacitance, a comparative CV study was carried out by synthesizing various DA-rGO xerogels with different ratios (w/w) of DA to GO *via* hydrothermal treatment followed by potential cycling and the results are presented in Fig. S12c.† A strong dependence between the initial DA loading in the hybrid material and capacitance was observed. The change in specific capacitance as a function of the DA weight ratio, at a scan rate of 100 mV s^{-1}, is shown in a bar diagram in Fig. S12d.† The highest C_{SP} (263 F g^{-1}) is observed with EpDA-rGO_{1-2} mass loading. Therefore, a detailed electrochemical analysis of the optimized EpDA-rGO_{1-2} material was carried out. Fig. S12e† demonstrates the effect of varying DA concentration on both the C_{SP} and rate capability of the electrodes at a sweep rate of 10–1000 mV s^{-1}. EpDA-rGO_{1-2} not only shows the highest C_{SP}, the rate capability of this particular composition is also the best. Even at a high scan rate of 1000 mV s^{-1}, it can retain 74% of its initial capacitance at 10 mV s^{-1}, demonstrating the excellent rate capability of the optimized material.

Galvanostatic charge–discharge (GCD) analysis was further carried out as the best practice method[44] to assess the advantage of the *in situ* potential cycling more precisely. The charge–discharge profile of the optimized EpDA-rGO_{1-2} (in a wide range of current densities; from 0.5 A g^{-1} to 500 A g^{-1}), as depicted in Fig. 6a, also corroborated the results obtained from CV. A highest C_{SP} of 348 F g^{-1} was achieved at a current density of 0.5 A g^{-1}. The shape of the discharge curve also suggests the pseudocapacitive contribution to the overall capacitance, with varying slopes from 0.9 V to 0.6 V (capacitive contribution) and 0.6 V to 0 V (faradaic contribution). Aiming for high energy density without compromising on rate capability was another aspect of our study, which was satisfied when a highest energy density of 48.26 W h kg^{-1} was also registered with EpDA-rGO_{1-2} at a current density of 0.5 A g^{-1}. The comparative Ragone plots of all the various compositions are collectively exhibited in Fig. S12f† that clearly shows the superior performance of EpDA-rGO_{1-2} in terms of both energy and power density.

The conductivity and ease of ionic transport of the EpDA-rGO_{1-2} electrode are further characterized by electrochemical impedance spectroscopy (EIS). As observed in the high frequency region of the Nyquist plot (Fig. S13a†), the small semi-circular region corresponding to the EpDA-rGO_{1-2} may stem from a negligible interfacial charge transfer resistance.[45] This confirms the high conductivity of the hybrid structure even after the incorporation of the DA moiety. Similarly, in the low

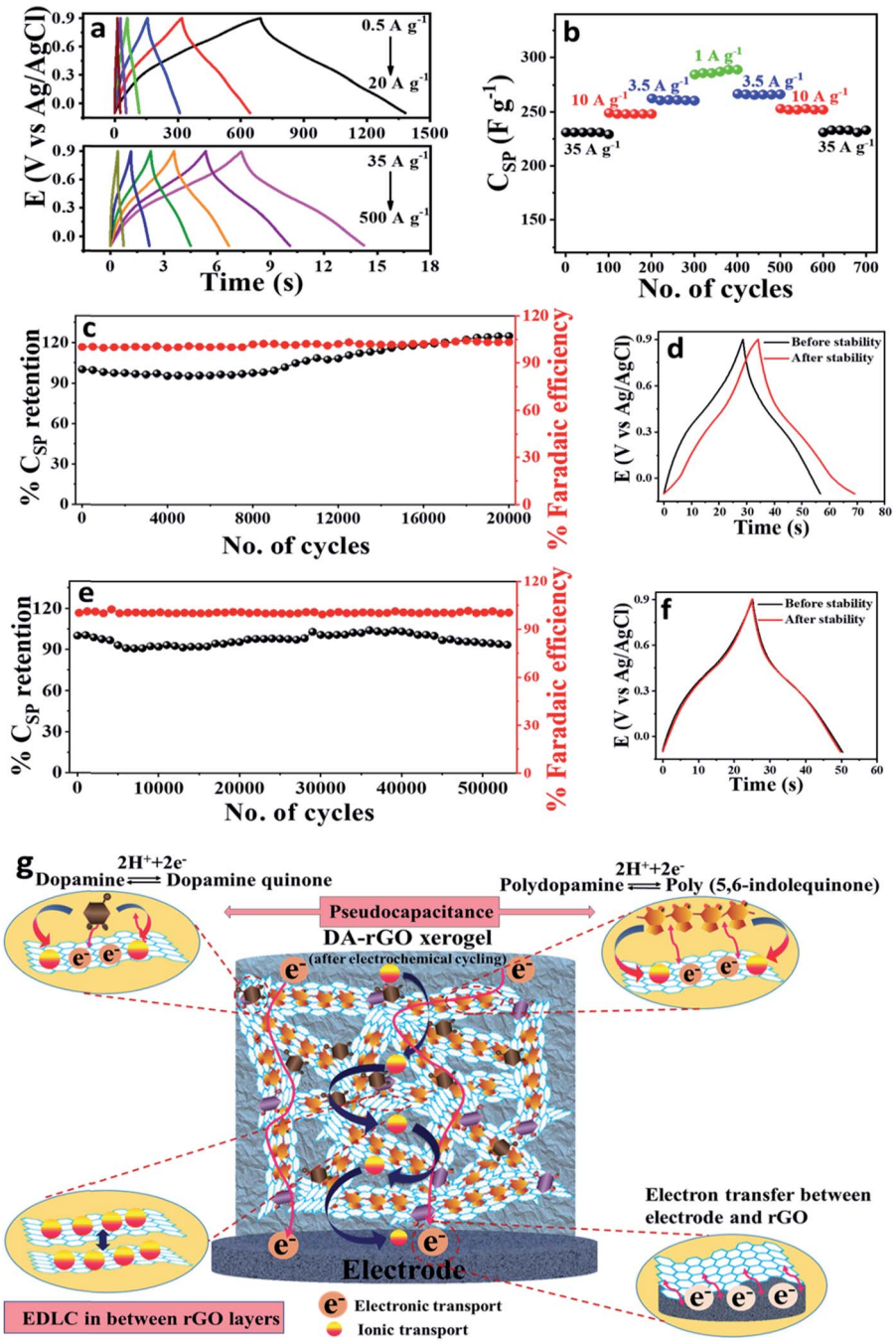

Fig. 6 Electrochemical characterization of the electrochemically *in situ* polymerized EpDA-rGO$_{1-2}$ samples in 1 M H_2SO_4 aqueous electrolyte. (a) Galvanostatic charge–discharge (GCD) profile at various current densities. (b) Continuous cycling stability study at various current densities for 100 charge–discharge cycles each to indicate rate capability and cycling reversibility. Cycling stability and retention of faradaic efficiency study at a current density of (c) 10 A g^{-1} for 20 000 cycles with an initial capacitance retention of 125% and (e) 35 A g^{-1} for 53 000 cycles with an initial capacitance retention of 94%. (d) and (f) show GCD analysis before and after the stability study. (g) Schematic illustration of the ionic and electronic transport taking place in the 3D network of the EpDA-rGO$_{1-2}$ structure.

frequency range, EpDA-rGO$_{1-2}$ shows slight deviation from the vertical line, as compared to the pristine rGO electrode, which may be ascribed to the increase of Warburg resistance due to the presence of the pseudocapacitive DA molecule between the rGO sheets. The dependence of the phase angle on the applied frequency was evaluated in the corresponding Bode plot, as exhibited in Fig. S13b.† The frequency at which the phase angle reaches 45° is known as the knee frequency (f_0), where the capacitive and resistive impedances are equal. The relaxation time ($\tau_0 = 1/f_0$) denotes the minimum time required to discharge all the energy from the storage system with an efficiency of greater than 50%.[46] The relaxation time for the EpDA-

rGO_{1-2} hybrid electrode (157 ms) was far less than that of the pristine rGO electrode (257 ms), indicating faster ion-transport indicating faster ion-transport indicating faster ion-transport kinetics and good electrical conductivity.

Cycling performance of EpDA-rGO_{1-2}. Hybrid materials with pseudocapacitive components often suffer from poor cycling stability because of the low conductivity and degradation of the redox moiety during continuous charge–discharge cycles. Although unlike other pseudocapacitive materials, the amount of buffer space available in the highly porous interconnected electro-active xerogel hybrid structure can release the stress caused by the volume change in the redox material during continuous charge–discharge cycles,[19] very few redox active carbon xerogels have achieved excellent cycling stability to date. Table 2 summarizes and compares the cycling performance of the EpDA-rGO_{1-2} electrode with various quinone-based redox supercapacitors. To establish the cycling reversibility of the EpDA-rGO electrode, initially we tested it at various current densities (1, 3.5, 10, and 35 A g^{-1}) for 100 cycles each continuously. Fig. 6b demonstrates that even after 100 charge–discharge cycles at each current density (descending followed by ascending order), the EpDA-rGO electrode possess excellent rate performance and ultra-strong capacitance reversibility. The charge–discharge profile of a pseudocapacitive system is more relevant at lower current densities to study its charge transport kinetics, as at lower current densities the redox process is more dominant. Therefore, EpDA-rGO was subjected to the cycling durability test at a sufficiently lower current density of 10 A g^{-1} as well for 20 000 GCD cycles (Fig. 6c), which exhibits around 125% of the initial capacitance retention. A slight enhancement in the specific capacitance can be observed after GCD cycling measurements (Fig. 6d) as a result of the increase in the active redox sites of the electrode surface. Fig. 6c also shows the retention of coulombic or faradaic efficiency around 103.2% indicating a slight involvement of faradaic processes during the GCD cycling test. Therefore, instigated by the excellent capacitance retention at 10 A g^{-1}, the cycling durability of the EpDA-rGO_{1-2} electrode was investigated at further lower current densities (1 and 3.5 A g^{-1}) for various galvanostatic charge–discharge cycles (500 and 2000 cycles, respectively) (Fig. S14†). The inset of all the stability plots in Fig. S14† represents the charge–discharge scans before and after the stability study. On the other hand, the rate capability and power delivery of a supercapacitor system are always best evaluated by its performance at higher current densities, where the charge–discharge process is very fast. Fig. 6d shows that 94% of the initial capacitance is retained by the EpDA-rGO_{1-2} electrode even after 53 000 continuous GCD cycles at a very high current density of 35 A g^{-1}. Interestingly, the EpDA-rGO_{1-2} electrode shows more than 93% retention of the initial capacitance at all the above-mentioned current densities, promoting it as the most versatile pseudocapacitors reported till date, for commercial use. It exceeds the cycling stability of various xerogel materials, for example – DMQ@rGO (99% C_{SP} retention after 25 000 CV cycles at 5 mV s^{-1}),[6] PDA-rGO (99% C_{SP} retention after 10 000 GCD cycles at 2 A g^{-1})[47] or AQS@rGO (89.1% after 10 000 GCD cycles at 10 A g^{-1}).[7] It even surpasses the cycling stability of a recently reported carbon-CP composite material, PVA/G/PAni-4C/G, showing 82% capacitance retention after 50 000 continuous GCD cycles[19] (Table 2). The impressive cycling stability may be attributed to a number of reasons: (a) the unique 3D interconnected porous architecture with uniform distribution of the DA moiety that ensured a continuous conductive pathway for rapid charge-transfer kinetics without the depletion of the electrode material in the electrolyte; (b) covalent interaction of the DA moiety to the rGO sheet *via* the amide linkage, which not only provides higher charge accumulation and a depletion region as compared to only π–π interactions, but also prevents the aggregation and degradation of the organic molecule during rigorous charge–discharge cycling; (c) *in situ* electropolymerization also plays a dynamic role in enhancing the charge-distribution on the rGO surface *via* the formation of EpDA therefore effectively preventing the parasitic side reactions and enhancing the cycle-life; (d) the basal plane of the rGO sheets provides excellent mechanical stability and conductivity that ensured continuous electronic channels even at high current density for stable electrochemical performances. GCD curves before and after 53 000 cycles are exhibited in Fig. 6d that clearly shows that the shape of the curve remains intact with negligible decay in the discharge

Table 2 Comparison of the cycling stability of the EpDA-rGO xerogel with other reported contemporary quinone-based redox supercapacitors as well as other composite pseudocapacitors[a]

Material	Electrolyte	% Retention (cycle number)	Scan-rate, current density	References
EpDA-rGO	H_2SO_4	94% (53 000)	35 A g^{-1}	This work
PQ-OLC	H_2SO_4	97% (10 000)	1.3 A g^{-1}	50
DMQ@rGO	H_2SO_4	99% (25 000)	50 mV s^{-1}	6
AQS@rGO	H_2SO_4	89.1% (10 000)	10 A g^{-1}	7
Th-GA	H_2SO_4	91% (10 000)	10 A g^{-1}	8
PVA/G/PAni-4C/G	H_2SO_4	82% (50 000)	50 mA	19
Ex-GF/PPy-NDS	KCl	82% (1000)	5 A g^{-1}	54
Co_3O_4/GNS	KOH	70% (4000)	0.2 A g^{-1}	53

[a] EpDA – electropolymerized dopamine; rGO – reduced graphene oxide; PQ – 9,10-phenanthrenequinone; OLC – onion-like carbon; DMQ – 2,5-dimethoxy-1,4-benzoquinone; AQS – anthraquinone-2-sulfonate; Th – thionine; GA – graphene aerogel; PVA – polyvinyl alcohol; G – graphene; PANI – polyaniline; PPy – polypyrrole; Ex-GF – exfoliated graphite foil; NDS – 1,5-naphthalene disulphonate; GNS – graphene nanosheets.

time, indicating excellent integration of the active electrode material onto the substrate surface. Fig. 6d also shows the retention of coulombic or faradaic efficiency around 100.4% indicating an absence of any side reactions or faradaic processes during the GCD cycling test.

Proposed charge-storage mechanism in the EpDA-rGO$_{1\text{-}2}$ electrode material. In order to explain the superior performance of the *in situ* EpDA-rGO$_{1\text{-}2}$ electrode material, a schematic illustration of the plausible mechanism of the charge–discharge phenomenon in the material as well as the material–electrode interface is exhibited in Fig. 6g. The cross-linked xerogel architecture is an excellent example to show both electrochemical double layer capacitance (EDLC) owing to the graphene base (bottom panel of Fig. 6g) and pseudocapacitance due to the availability of two redox active species, DA and pDA, which undergo two-proton coupled reactions to append to the faradaic contribution together (top panel of Fig. 6g). On the other hand, *in situ* conversion of the DA species to EpDA maximizes the surface coverage *via* non-covalent π–π interactions, enhancing the active redox sites resulting in improved gravimetric capacitance. Moreover, covalent cross-linking helps to achieve a highly interconnected three-dimensional xerogel architecture that possesses a lot of buffer space in between to allow faster movement of the electrolyte ions through the pores. Therefore, the availability of porous interconnected architecture in covalently linked EpDA-rGO greatly promotes faster charge-transport kinetics thereby improving the ionic conductivity. Interestingly, the unique synthesis approach combining both covalent and non-covalent interactions maximizes electronic (*via* non-covalent π–π interactions) as well as ionic transport (through the pores), providing faster redox kinetics and high energy and power density.

Electrochemical performances in device architecture. To further investigate the superior performance of the EpDA-rGO$_{1\text{-}2}$ electrode for practical applications, an all-solid-state self-supported symmetric supercapacitor was developed. The fabrication procedure is described in detail in the ESI† (see the Experimental section). All-solid-state supercapacitors are lightweight, safe and portable storage systems that can be integrated into small electronic devices as power sources. In order to achieve the maximum operating voltage of the as-fabricated EpDA-rGO//EpDA-rGO device, cyclic voltammetric responses were recorded at various cell voltages starting from 0.8 to 1.2 V. An increase in the faradaic current in a higher scanning working voltage window (1.1 V and 1.2 V) indicates some faradaic processes that may interfere in the stability of the device during long service hours[48] and therefore, the optimum working voltage window was chosen as 1 V (Fig. S15a†). The cyclic voltammograms of the device at various scan rates (5–50 mV s^{-1}) are exhibited in Fig. 7a. The shape of the voltammograms was maintained even at higher scan rates, indicating the good rate capability of the EpDA-rGO material even in the device. To gain more insight into the charge-storage capacity of the device, GCD profiles were also recorded at various current densities from

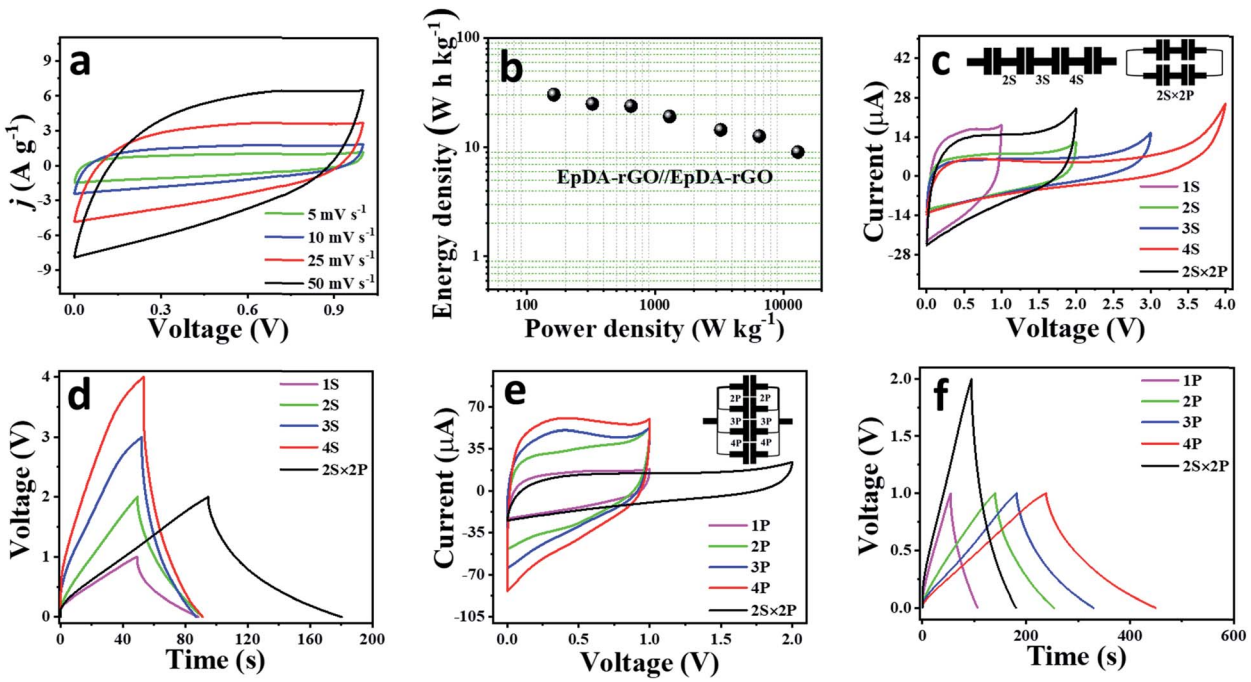

Fig. 7 (a) Cyclic voltammograms at various scan rates of the symmetric all-solid-state planar device, EpDA-rGO//EpDA-rGO in 1 M PVA/H_2SO_4 solid state gel electrolyte. (b) Ragone plot of the device. (c)–(e) Integration of such planar devices in various series and parallel combinations and their electrochemical response. (c) CV curves at a scan rate of 10 mV s^{-1} and (d) GCD profiles at a current density of 2.6 A g^{-1} obtained from series (1S to 4S) as well as the 2S × 2P configuration, the inset of (c) showing the schematic representation of the linear devices arranged in series and 2S × 2P configurations. Similarly (e) and (f) show CV and GCD responses of the devices respectively, arranged in parallel (1P to 4P), compared with the 2S × 2P configuration, the inset of (e) showing the schematic representation of the linear devices arranged in the parallel configuration.

0.325 to 13 A g^{-1} (Fig. S15b†). The symmetric shape of the GCD curves and low ohmic drop indicate excellent rate performance (Fig. S15c†) as well as negligible internal resistance in the device. A highest C_{SP} of 218.1 F g^{-1} was obtained for the device at a current density of 0.325 A g^{-1}, which is higher than or almost comparable to those of previously reported state-of-the-art solid-state symmetric devices (Table S2†). For planar solid-state supercapacitors, the areal or volumetric specific capacitance is a more reliable evaluation parameter than gravimetric capacitance. Through cross-sectional SEM images (Fig. S15d,† inset), the average thickness of the material in the symmetric device was calculated to be around 1.022 μm. Therefore, the areal capacitance was calculated to be 52 mF cm^{-2} at a current density of 78 μA cm^{-2}, while the volumetric capacitance was calculated to be 509 mF cm^{-3} at the same current density. The energy and power density are the two main crucial parameters in determining the practical application of any supercapacitor device. There has always been a demand for noble pseudocapacitive materials that can achieve both high energy and high-power density. Therefore, the Ragone plot was devised for our as-fabricated EpDA-rGO//EpDA-rGO solid-state device and is exhibited in Fig. 7b. A highest energy density of 30.3 W h kg^{-1} was obtained at a power density of 1630 W kg^{-1}, while a highest power delivery of 13 020 W kg^{-1} was achieved even while maintaining the specific energy at 9.04 W h kg^{-1}. A highest volumetric energy density of 70.7 W h L^{-1} with a highest power density of 30.57 W L^{-1} was measured based on the thickness of the material in the device. In order to further demonstrate the excellent storage performance as well as instant power delivery capacity of our as-fabricated device, Ragone plot comparison has been drawn with some previously reported graphene hydrogel/aerogel based solid state devices and is depicted in Fig. S15e.† It shows much superior energy as well as power density as compared to LS-GHs (13.8 W h kg^{-1}, 5000 W kg^{-1}),[49] BN-GAs (8.7 h kg^{-1}, 1650 W kg^{-1})[50] and OMC-GAs (6.2 W h kg^{-1}, 3545 W kg^{-1}).[51] A detailed comparative electrochemical performance analysis to contemporary composite pseudocapacitors including CPs, metal-oxides and similar organic redox centre-based xerogel materials as well as devices is provided in Table S2.† The EpDA-rGO_{1-2} electrode material exhibits a highest energy density of 48.26 W h kg^{-1} and the EpDA-rGO//EpDA-rGO symmetric solid-state device shows a highest energy density of 30.3 W h kg^{-1}, much higher than those of most of the reported organic electro-active xerogel pseudocapacitors, for example – AZ-SHGs (18.2 W h kg^{-1}),[5] PQ-OLCs (4.5 W h kg^{-1}),[52] AQ@CFs (19.3 W h kg^{-1}),[53] PPD-C-DCNTs (19.1 W h kg^{-1}),[14] *etc.* It even shows superior or almost comparable energy density to those of mostly reported carbon-CP composites, for example – PANI-graphene foam (43.64 W h kg^{-1})[54] or carbon-TMO composite structures, like Co_3O_4/GNS (21.9 W h kg^{-1}),[55] *etc.* Although there have been some reports mentioning higher energy density, for instance – DMQ@rGO xerogel (113.4 W h kg^{-1}),[6] or composites of carbon-CPs, like – Ex-GF/PPy-NDS (82.4 W h kg^{-1})[56] or PAG80 (66.67 W h kg^{-1}),[57] the solid-state symmetric device shows an excellent power delivery of 13.02 kW kg^{-1}, which is better than those of most of the reported two-electrode systems. For example – AZ-SHGs (0.7 kW kg^{-1}),[5] PPD-C-DCNTs (0.8 kW kg^{-1}),[14] TH-GAs (8.7 kW kg^{-1}),[8] or Ex-GF/PPy-NDS (13 kW kg^{-1})[56] or Co_3O_4/GNS (2.19 kW kg^{-1}).[55] Our EpDA-rGO_{1-2} electrode demonstrates excellent electrochemical activity due to an enhanced ionic and electronic conductivity coming from a novel synthesis strategy of both covalent and non-covalent interactions.

The fact that the specific energy and power delivery capability of a single device are often not sufficient to run commercial devices, it is generally preferred to package the cells in various series and parallel arrangements or a combination of both to meet the energy and power requirements.[58] To meet the demand of high voltage, four as-fabricated solid-state linear devices were arranged in series, while to improve the current response and capacitance, they were connected in a parallel configuration. The electrochemical performance of the tandem devices was investigated in terms of their CV and GCD responses. As can be observed in Fig. 7c and d, the series combination of four devices exhibited an enhanced potential window of 4 V as compared to 1 V of a single device. The inset of Fig. 7c schematically shows the series configuration of the four devices. Similarly, when arranged in a parallel fashion, the tandem configuration shows an almost 4-fold increase in the current response as compared to a single device both in CV (Fig. 7e) and GCD (Fig. 7f) profiles. The inset of Fig. 7e schematically shows the parallel configuration of the four devices. It is highly required that by the tandem configuration of the individual cells, the highest current response is attained in the highest operating potential window, leading to minimum energy loss. Therefore, the performances of the four devices were also evaluated by arranging two of them in series and then connecting the two series devices in a parallel fashion (2S × 2P configuration). As expected, the 2S × 2P tandem configuration shows an enhanced potential window of 2 V while improving the current response to 2-fold as compared to two devices in series (Fig. 7c–f).

One of the most routine features of any commercial device is to have a long service-life. Based on the unprecedented cycling performance of our active electrode material; it was highly anticipated that the symmetric solid-state device, EpDA-rGO//EpDA-rGO will eventually show excellent cycling stability. However, in a solid-state gel electrolyte, the increased resistance at the electrolyte–electrode interface hampers the rate performance and eventually the device performance suffers with continuous charge–discharge cycles. In spite of this, in Fig. 8a, the device shows a remarkable capacitance retention of 92% even after 10 000 continuous GCD cycles at a very high current density of 10 A g^{-1}, which is much superior to those of most of the gel-electrolyte based pseudocapacitors reported to date, for example – LS-GHs (84% (10 000) @ 2 A g^{-1})[49] or rGO/MoO_3 (80% (5000) @ 2 A g^{-1})[59] (Table S2†). Fig. 8a also shows the retention of coulombic efficiency around 100% indicating an absence of any side reactions during the GCD cycling test. The inset of Fig. 8a shows the first and last four cycles revealing almost unchanged GCD profiles, indicating negligible ohmic drop in the device.

To endorse the development of self-supported metal free light-weight supercapacitors for portable electronic

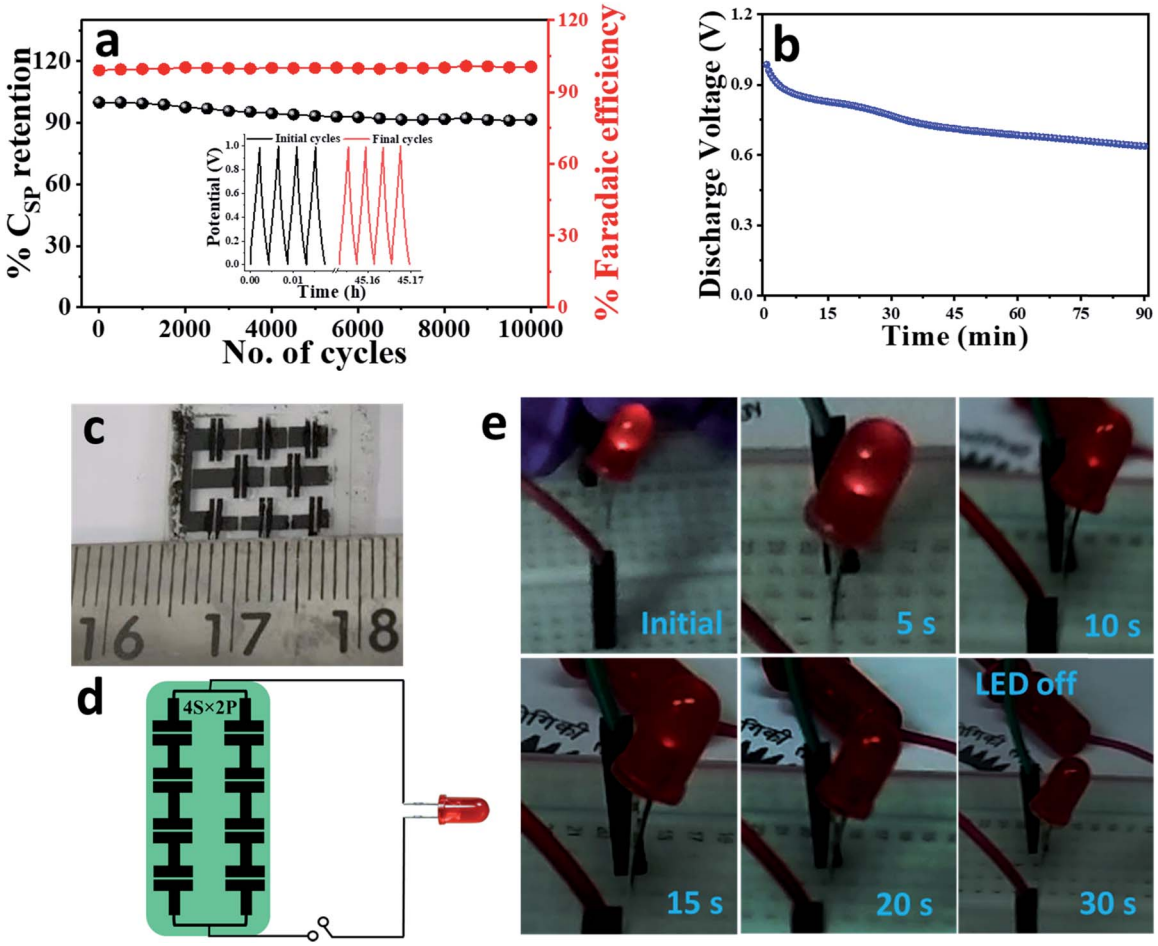

Fig. 8 (a) Percentage capacitance retention (92%) as well as faradaic efficiency of the solid-state device, EpDA-rGO//EpDA-rGO after 10 000 continuous cycles at a high current density of 10 A g^{-1}, the inset showing GCD profiles of the first and last four cycles. (b) Self-discharge study of a single charged supercapacitor device. (c) Digital photograph of the laser-patterned linear devices. (d) Integration of the devices in a 4S × 2P array exhibited schematically for powering up an LED. (e) Digital images showing the lighting of a single LED device for 30 s after charging the module in (d) at 4 V for 1 minute.

applications, a number of studies were performed with the EpDA-rGO//EpDA-rGO device as a power source. At first, the discharging performance of a single device was evaluated by charging it at 3 V for 3 minutes using a commercial DC power source. Self-discharge is a valuable performance metric and of major practical significance for pseudocapacitors. After 3 minutes, the device was able to sustain almost 70% of the cell voltage even after 1.5 h. Fig. 8b shows the discharge voltage profile of the device as a function of time. The device performance was also validated by its ability to power up a commercial 1.6 V LED system. The digital image of the as-patterned in-plane devices is shown in Fig. 8c. The devices were arranged in a 4S × 2P tandem configuration as schematically shown in Fig. 8d and then charged at 4 V for 1 minute. As can be seen in Fig. 8e, after charging, the tandem system was able to power up the LED for 30 seconds continuously, demonstrating the practical viability of the EpDA-rGO//EpDA-rGO symmetric device.

The overall material as well as device performance as a pseudocapacitor promotes EpDA-rGO as a potential future storage material, ready to be employed in commercial supercapacitors.

Conclusions

In summary, a unique combination of covalent and non-covalent functionalization of rGO *via* an organic redox species, dopamine (DA) has been explored to develop a high-rate pseudocapacitor with outstanding cycle-life. The availability of two electron donating groups, *i.e.*, hydroxyl and alkyl amine functionalities at the *para* positions in the DA molecule promotes its easy covalent interaction with rGO, during the hydrothermal reduction process, whereas the aromatic π cloud helps in non-covalent interaction or molecular level binding; which was further confirmed by theoretical DFT analysis. Additionally, in this study, we have also explored the well-known polymerization tendency of DA to form pDA by cycling the xerogel material in the experimental electrolyte and generating the *in situ* EpDA-rGO xerogel material. Among various tested electrodes, EpDA-$rGO_{1\text{-}2}$ exhibits the highest specific

capacitance of 348 F g^{-1} at a current density of 0.5 A g^{-1}. *In situ* electro-polymerization induces large charge-distribution over the rGO surface *via* the formation of EpDA, preventing the parasitic side reactions of the organic species and leading to an outstanding cycling stability of 94% after 53 000 continuous GCD cycles at 35 A g^{-1}. Additionally, an all-solid-state symmetric planar supercapacitor device was fabricated using the EpDA-$rGO_{1\text{-}2}$ active electrode material, which delivers an exceptional energy density of 30.3 W h kg^{-1}, one of the highest specific energies delivered by solid-state symmetric graphene hydrogel/aerogel-based pseudocapacitors, reported to date. Even the device shows an exceptional cycling stability of 92% after 10 000 GCD cycles at a very high current density of 10 A g^{-1}. The combined output from both the theoretical study and experimental findings helps us to conclude that the careful selection of the organic moiety ensures optimum interaction with the conductive substrate which in turn helps in addressing the cycling performance of pseudocapacitors. This work is a unique attempt to study the mechanism of redox supercapacitors at the molecular level and offers new insights into how to improve the long-standing issue of stability and inferior power output of pseudocapacitors. It may promote future research in the field of organic pseudocapacitors as suitable candidates for commercial applications.

Conflicts of interest

There are no conflicts to declare.

Acknowledgements

TP acknowledges DST INSPIRE and CSIR SRF for providing a fellowship and Panjab University for Ph. D. registration. This work was financially supported by DST INSPIRE (DST/INSPIRE/04/2015/000337) and DST SERB EMR (EMR/2016/000040). The authors acknowledge INST, Mohali for instrumental support. Our sincere thanks are extended to CDAC, Pune's supercomputing resources on PARAM YUVA II for theoretical calculations.

Notes and references

1 M. Kim, C. Lee and J. Jang, *Adv. Funct. Mater.*, 2014, **24**, 2489–2499.
2 A. Jaffe, A. Saldivar Valdes and H. I. Karunadasa, *Chem. Mater.*, 2015, **27**, 3568–3571.
3 V. Augustyn, P. Simon and B. Dunn, *Energy Environ. Sci.*, 2014, **7**, 1597–1614.
4 L. Madec, A. Bouvrée, P. Blanchard, C. Cougnon, T. Brousse, B. Lestriez, D. Guyomard and J. Gaubicher, *Energy Environ. Sci.*, 2012, **5**, 5379–5386.
5 N. An, Y. An, Z. Hu, B. Guo, Y. Yang and Z. Lei, *J. Mater. Chem. A*, 2015, **3**, 22239–22246.
6 M. Boota, C. Chen, M. Bécuwe, L. Miao and Y. Gogotsi, *Energy Environ. Sci.*, 2016, **9**, 2586–2594.
7 R. Shi, C. Han, H. Duan, L. Xu, D. Zhou, H. Li, J. Li, F. Kang, B. Li and G. Wang, *Adv. Energy Mater.*, 2018, **8**, 1802088.
8 Y. Shabangoli, M. S. Rahmanifar, M. F. El-Kady, A. Noori, M. F. Mousavi and R. B. Kaner, *Adv. Energy Mater.*, 2018, **8**, 1802869.
9 T. Tomai, S. Mitani, D. Komatsu, Y. Kawaguchi and I. Honma, *Sci. Rep.*, 2014, **4**, 1–6.
10 A. Yu, A. Davies and Z. Chen, in *Electrochemical Technologies for Energy Storage and Conversion*, Wiley-VCH Verlag GmbH & Co. KGaA, Weinheim, Germany, 2012, 1st edn, pp. 317–382.
11 Y. Liang, Z. Tao and J. Chen, *Adv. Energy Mater.*, 2012, **2**, 742–769.
12 K. Kalinathan, D. P. DesRoches, X. Liu and P. G. Pickup, *J. Power Sources*, 2008, **181**, 182–185.
13 G. Pognon, C. Cougnon, D. Mayilukila and D. Bélanger, *ACS Appl. Mater. Interfaces*, 2012, **4**, 3788–3796.
14 Y. He, X. Yang, N. An, X. Wang, Y. Yang and Z.-A. Hu, *New J. Chem.*, 2019, **43**, 1688–1698.
15 Q. Wu, Y. Sun, H. Bai and G. Shi, *Phys. Chem. Chem. Phys.*, 2011, **13**, 11193–11198.
16 L. Hamenu, A. Madzvamuse, L. Mohammed, M. Hu, J. Park, M. H. Ryou, Y. M. Lee and J. M. Ko, *Synth. Met.*, 2017, **231**, 25–33.
17 S. Roldán, M. Granda, R. Menéndez, R. Santamaría and C. Blanco, *J. Phys. Chem. C*, 2011, **115**, 17606–17611.
18 S. Roldán, C. Blanco, M. Granda, R. Menéndez and R. Santamaría, *Angew. Chem., Int. Ed.*, 2011, **50**, 1699–1701.
19 A. Khosrozadeh, G. Singh, Q. Wang, G. Luo and M. Xing, *J. Mater. Chem. A*, 2018, **6**, 21064–21077.
20 T. Purkait, G. Singh, N. Kamboj, M. Das and R. S. Dey, *J. Mater. Chem. A*, 2018, **6**, 22858–22869.
21 R. S. Dey, H. A. Hjuler and Q. Chi, *J. Mater. Chem. A*, 2015, **3**, 6324–6329.
22 L. Q. Xu, W. J. Yang, K. G. Neoh, E. T. Kang and G. D. Fu, *Macromolecules*, 2010, **43**, 8336–8339.
23 T. Yadav and V. Mukherjee, *J. Mol. Struct.*, 2018, **1160**, 256–270.
24 J. E. Carter, J. H. Johnson and D. M. Baaske, *Anal. Profiles Drug Subst. Excipients*, 1982, **11**, 257–272.
25 R. A. Zangmeister, T. A. Morris and M. J. Tarlov, *Langmuir*, 2013, **29**, 8619–8628.
26 X. Jian, H. min Yang, J. gang Li, E. hui Zhang, L. le Cao and Z. hai Liang, *Electrochim. Acta*, 2017, **228**, 483–493.
27 E. Desimoni and B. Brunetti, *Chemosensors*, 2015, **3**, 70–117.
28 H. Gao, Y. Sun, J. Zhou, R. Xu and H. Duan, *ACS Appl. Mater. Interfaces*, 2013, **5**, 425–432.
29 F. Bernsmann, A. Ponche, C. Ringwald, J. Hemmerlé, J. Raya, B. Bechinger, J.-C. Voegel, P. Schaaf and V. Ball, *J. Phys. Chem. C*, 2009, **113**, 8234–8242.
30 R. S. Dey, S. Hajra, R. K. Sahu, C. R. Raj and M. K. Panigrahi, *Chem. Commun.*, 2012, **48**, 1787.
31 V. K. Thakur, M. F. Lin, E. J. Tan and P. S. Lee, *J. Mater. Chem.*, 2012, **22**, 5951–5959.
32 M. J. Frisch, G. W. Trucks, H. B. Schlegel, G. E. Scuseria, M. A. Robb, J. R. Cheeseman, G. Scalmani, V. Barone, G. A. Petersson, H. Nakatsuji, X. Li, M. Caricato, A. V. Marenich, J. Bloino, B. G. Janesko, R. Gomperts and B. Me, *Gaussian 16, Revision B. 01*, 2016, 1.

33 R. Dennington, T. A. Keith and J. M. Millam, *GaussView, Version 6.1*, 2016.
34 D. García-Toral, M. González-Melchor, J. F. Rivas-Silva, E. Meneses-Juárez, J. Cano-Ordaz and G. H. Cocoletzi, *J. Phys. Chem. B*, 2018, **122**, 5885–5896.
35 J. lei Wang, B. chao Li, Z. jun Li, K. feng Ren, L. jiang Jin, S. miao Zhang, H. Chang, Y. xin Sun and J. Ji, *Biomaterials*, 2014, **35**, 7679–7689.
36 M. D. Hawley, S. V. Tatawawadi, S. Piekarski and R. N. Adams, *J. Am. Chem. Soc.*, 1967, **89**, 447–450.
37 T. C. Liu, W. G. Pell, B. E. Conway and S. L. Roberson, *J. Electrochem. Soc.*, 1998, **145**, 1882.
38 S. Ardizzone, G. Fregonara and S. Trasatti, *Electrochim. Acta*, 1990, **35**, 263–267.
39 V. Augustyn, J. Come, M. A. Lowe, J. W. Kim, P.-L. Taberna, S. H. Tolbert, H. D. Abruña, P. Simon and B. Dunn, *Nat. Mater.*, 2013, **12**, 518–522.
40 T. Brousse, D. Bélanger and J. W. Long, *J. Electrochem. Soc.*, 2015, **162**, A5185–A5189.
41 V. Krishnakumar and R. John Xavier, *Spectrochim. Acta, Part A*, 2004, **60**, 709–714.
42 L. E. Clougherty, J. A. Sousa and G. M. Wyman, *J. Org. Chem.*, 1957, **22**, 462.
43 T. Noguchi, Y. Inoue and X. S. Tang, *Biochemistry*, 1999, **38**, 399–403.
44 M. D. Stoller and R. S. Ruoff, *Energy Environ. Sci.*, 2010, **3**, 1294–1301.
45 Q. Wu, Y. Xu, Z. Yao, A. Liu and G. Shi, *ACS Nano*, 2010, **4**, 1963–1970.
46 W. Liu, C. Lu, H. Li, R. Y. Tay, L. Sun, X. Wang, W. L. Chow, X. Wang, B. K. Tay, Z. Chen, J. Yan, K. Feng, G. Lui, R. Tjandra, L. Rasenthiram, G. Chiu and A. Yu, *J. Mater. Chem. A*, 2016, **4**, 3754–3764.
47 S. Dong, Z. Xie, Y. Fang, K. Zhu, Y. Gao, G. Wang, J. Yan, K. Cheng, K. Ye and D. Cao, *ChemistrySelect*, 2019, **4**, 2711–2715.
48 Z. Dai, C. Peng, J. H. Chae, K. C. Ng and G. Z. Chen, *Sci. Rep.*, 2015, **5**, 9854.
49 F. Li, X. Wang and R. Sun, *J. Mater. Chem. A*, 2017, **5**, 20643–20650.
50 Z. S. Wu, A. Winter, L. Chen, Y. Sun, A. Turchanin, X. Feng and K. Müllen, *Adv. Mater.*, 2012, **24**, 5130–5135.
51 R. Liu, L. Wan, S. Liu, L. Pan, D. Wu and D. Zhao, *Adv. Funct. Mater.*, 2015, **25**, 526–533.
52 D. M. Anjos, J. K. McDonough, E. Perre, G. M. Brown, S. H. Overbury, Y. Gogotsi and V. Presser, *Nano Energy*, 2013, **2**, 702–712.
53 H. Wang, H. Yi, C. Zhu, X. Wang and H. Jin Fan, *Nano Energy*, 2015, **13**, 658–669.
54 Y. Xu, Y. Tao, X. Zheng, H. Ma, J. Luo, F. Kang and Q. H. Yang, *Adv. Mater.*, 2015, **27**, 8082–8087.
55 Q. Guan, J. Cheng, B. Wang, W. Ni, G. Gu, X. Li, L. Huang, G. Yang and F. Nie, *ACS Appl. Mater. Interfaces*, 2014, **6**, 7626–7632.
56 Y. Song, J. L. Xu and X. X. Liu, *J. Power Sources*, 2014, **249**, 48–58.
57 K. Zhang, L. L. Zhang, X. S. Zhao and J. Wu, *Chem. Mater.*, 2010, **22**, 1392–1401.
58 N. Kamboj, T. Purkait, M. Das, S. Sarkar, K. S. Hazra and R. S. Dey, *Energy Environ. Sci.*, 2019, **12**, 2507–2517.
59 X. Cao, B. Zheng, W. Shi, J. Yang, Z. Fan, Z. Luo, X. Rui, B. Chen, Q. Yan and H. Zhang, *Adv. Mater.*, 2015, **27**, 4695–4701.